Toward Extending Concentric Tube Robot Kinematics for Large Clearance and Impulse Curvature

Zhouyu Zhang*, Jia Shen*, Junhyoung Ha, and Yue Chen

arXiv:2308.10770v1 [cs.RO] 21 Aug 2023

Abstract—**Concentric Tube Robots (CTRs) have been proposed to operate within the unstructured environment for minimally invasive surgeries. In this letter, we consider the operation scenario where the tubes travel inside the channels with a large clearance or large curvature, such as aortas or industrial pipes. Accurate kinematic modeling of CTRs is required for the development of advanced control and sensing algorithms. To this end, we extended the conventional CTR kinematics model to a more general case with large tube-to-tube clearance and large centerline curvature. Numerical simulations and experimental validations are conducted to compare our model with respect to the conventional CTR kinematic model. In the physical experiments, our proposed model achieved a tip position error of 1.53 mm in the 2D planer case and 4.36 mm in 3D case, outperforming the state-of-the-art model by 71% and 66%, respectively.**

Index Terms—**Concentric Tube Robot, Kinematic Modeling, Clearance, Curvature**

I. INTRODUCTION

Concentric tube robots (CTRs) are a class of continuum robots that have gained significant attention and progress in various fields, particularly in surgery and interventional medicine [1][2][3]. These robots are composed of multiple concentrically arranged super-elastic tubes, with each tube capable of independent actuation. By selectively controlling the linear translation and axial rotation of the tubes, CTRs can reconfigure themselves and generate tentacle-like motions to navigate through complex anatomical structures.

Accurate modeling of CTRs is of paramount importance for reliable manipulation. Cosserat rod theory has been extensively used to describe the kinematics of CTRs [4][5][6]. Prior work

indicated that the kinematics of CTRs involves formulating a set of differential equations with mixed boundary conditions [7], which are derived based on the idea of energy minimization or moment equilibrium. The boundary conditions at the base of the robot are the axial rotations and translations between the tubes, and the boundary conditions at the tip are vanishing internal moments. Numerical methods, such as the shooting method, have been employed to solve these differential equations. Additionally, the kinematic models have been extended to provide differential kinematics, such as inverse kinematics and Jacobian matrices, enabling real-time control of CTRs [8][9][10]. Recent efforts have also been put into the investigation of CTRs with external loading [6].

The presence of tube clearance can significantly affect the accuracy of CTRs as the assumption of concentricity may no longer hold true [6]. A recent numerical study indicated that the clearence could contribute up to 38.11% tip error when a miniature continuum robot deployed within a trocar that has a clearence of 0.25mm [11]. In 2017, co-author Dr. Ha took a pioneering step towards enhancing CTR modeling accuracy by incorporating the intertube clearance effect [12], [13]. Recently, [14] proposed the database method to compensate the error caused the intertube clearance. However, both approaches were evaluated with CTRs that have a relatively small clearance and smooth curvature.

In this letter, we present the latest results that extend upon the existing small clearance CTR kinematics model proposed in [12], [13] towards more intricate yet practical scenarios, which involve both large clearance and impulse curvature (see definition in Sec. II). This type of configuration is commonly observed in medical and engineering applications. For example, in medicine, a ∼2mm continuum catheter is maneuvered within the aorta that has a diameter of about 3cm [15]. In engineering applications, the continuum borescope is able to travel within the pipes that have a significantly larger clearance and impulse curvature on given locations (due to the pipe-pipe intersections with 90-degree elbows). The models in both operation scenarios can be approximated as the CTRs that have large clearance impulse curvature, where the aorta and pipe can be considered as the outer tube, and the continuum robot operate within can be considered as inner tube. Thus, the development of the CTR modeling with these considerations can facilitate the ubiquitous use of continuum robot in the more practical scenarios where the conventional CTR model fails, which forms the basic motivation of the proposed work.

The rest of this letter is formulated in the following struc-

ture. Part II presents the mathematical modeling of conventional zero clearance CTR, large clearance tube, and impulse curvature tube, respectively. In part III-A and III-B the models are validated both in simulations and experimental validations, followed by the conclusion in section IV.

II. CTR KINEMATIC MODELING

In this section, the conventional modeling of CTR is briefly discussed in Sec. II-A, and then extended by relaxing the requirement on tube-to-tube clearance and center line curvature. The modeling of the latter two cases can be combined, resulting in a large-clearance-impulse-curvature model (LCIC) to be discussed in Sec. II-B and Sec. II-C.

A. Standard Kinematics Model of CTRs

The kinematics of a single tube within the CTR labeled with index i can be obtained from the widely studied Cosserat rod model [6], which describes the evolution of the position and orientation by a system of ODEs. When concentricity constraint is ensured, the following ODEs (1) could be solved with boundary constraints imposed upon tip and base:

$$
\begin{aligned}
\mathbf{p}_i'(s) &= \mathbf{R}_i(s)\mathbf{e}_3 \\
\mathbf{R}_i'(s) &= \mathbf{R}_i(s)\left[\mathbf{u}_i(s)\right]_\times,
\end{aligned} \tag{1}
$$

where $\mathbf{e}_3 = [0\ 0\ 1]^T$, the prime operator $(\cdot)'$ denotes the derivative w.r.t. arc-length s, $\mathbf{p}_i(s)$, $\mathbf{R}_i(s)$, and $\mathbf{u}_i(s)$ are the centerline position, material coordinate frame, and 3D curvature vector of tube i at s, respectively, and $[\cdot]_\times$ represents the mapping from a 3D vector to the corresponding skew-symmetric matrix, i.e., the Lie algebra associated with the special orthogonal group SO(3). The curvature vector $\mathbf{u}_i(s)$ is determined by the elastic interaction between tubes. In the conventional kinematic models with strict concentricity assumption, the centerlines are identical between all tubes, i.e., $\mathbf{p}(s) = \mathbf{p}_1(s) = \mathbf{p}_2(s) = \cdots$. We refer the readers to [6] for more details.

B. Modeling of CTRs with Large Clearance

In the practical implementations of CTRs, the clearances between tubes are required to enable the relative rotation and translation with respect to each other. A more accurate model of CTRs can be obtained by relaxing the concentricity constraint (see Fig. 1-(a)). In this case, the centerlines of the tubes are no longer identical and will be obtained below.

To formulate the kinematics as a finite-dimensional problem, the centerline position and curvature are discretized along the arc length into virtual segments for each tube. The state variables of tube i are the concatenated vectors of discrete variables, given as

$$
\mathbf{u}^i = [\mathbf{u}_i(s_1)^T, \dots, \mathbf{u}_i(s_{N_i})^T]^T, \quad \mathbf{p}^i = [\mathbf{p}_i(s_1)^T, \dots, \mathbf{p}_i(s_{N_i})^T]^T, \tag{2}
$$

where s_j is the arc length of the j-th discretization point along the tube, and N_i is the total number of discretization. The state variables of the whole system is defined as concatenation of each tube variables

$$
\mathbf{u} = [\mathbf{u}^{1^T}, \dots, \mathbf{u}^{n^T}]^T, \quad \mathbf{p} = [\mathbf{p}^{1^T}, \dots, \mathbf{p}^{n^T}]^T. \tag{3}
$$
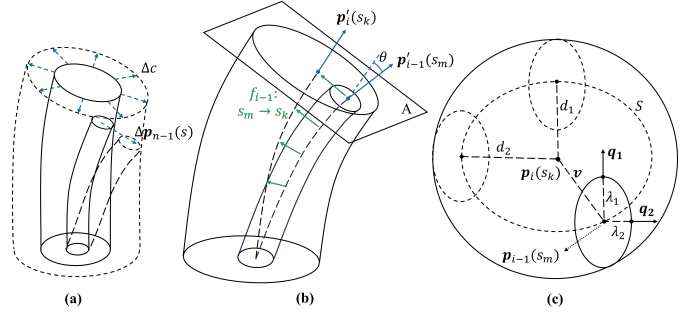
Fig. 1. Geometric relations between two adjacent tubes. (a) The change of the inner tube position as the clearance increases even the actuator-space translation and rotation remain constant. (b) The tangent vectors of the tube centerlines at a common cross-section. The mapping f is also displayed (in green) that finds the corresponding points on the outer tube closest to the inner tube. (c) A detailed illustration of the cross-section plane, labeled as plane A, that is in perpendicular to the outer tube,

where n is the number of the tubes. Letting $\mathbf{K}_i^{3\times 3}$ and $\hat{\mathbf{u}}_i(s)$ denote the 3×3 stiffness matrix and 3D precurvature vector of tube i [16], respectively, similar concatenations are possible to define $\mathbf{K}_i$, $\hat{\mathbf{u}}^i$, and $\hat{\mathbf{u}}$:

$$
\begin{aligned}
\mathbf{K}_i &= \mathrm{diag}(\mathbf{K}_i^{3\times 3}, \dots, \mathbf{K}_i^{3\times 3}) \in R^{3N_i \times 3N_i}, \\
\hat{\mathbf{u}}^i &= [\hat{\mathbf{u}}_i(s_1)^T, \dots, \hat{\mathbf{u}}_i(s_{N_i})^T]^T, \quad \hat{\mathbf{u}} = [\hat{\mathbf{u}}^{1^T}, \dots, \hat{\mathbf{u}}^{n^T}]^T.
\end{aligned} \tag{4}
$$

Subsequently, the elastic potential energy of tube i is expressed as

$$
E_p(\mathbf{u}^i, \hat{\mathbf{u}}^i, \mathbf{K}_i) = \frac{1}{2}(\mathbf{u}^i - \hat{\mathbf{u}}^i)^T \mathbf{K}_i (\mathbf{u}^i - \hat{\mathbf{u}}^i). \tag{5}
$$

In the absence of external forces and friction, the shapes of tubes are dominated by the stable equilibrium of the elastic potential energy (i.e., a local minimum). Accordingly, we formulate our large-clearance kinematics model as an energy minimization process subject to tube contact constraints:

$$
\min_{\mathbf{u}_i} \quad \sum_{i=1}^{n} E_P(\mathbf{u}_i) \tag{6a}
$$

$$
\text{s.t.} \quad C(\mathbf{p}_{i-1}, \mathbf{p}_i) \leq \mathbf{0} \text{ for } i = 2, \dots, n, \tag{6b}
$$

$$
\mathbf{p}_i = F(\mathbf{u}_i) \tag{6c}
$$

where $C(\mathbf{p}_{i-1}, \mathbf{p}_i)$ is the contact constraints with which the centerlines of any two adjacent tubes must comply, and $F(\cdot)$ integrates (1) to calculate $\mathbf{p}_i$ using $\mathbf{u}_i$.

Noting that tube i is the outer tube, tube $i-1$ is the adjacent inner tube, the contact constraint can be derived geometrically by considering the cross-section of tube i at $\mathbf{p}_i(s)$, labeled as plane A in Fig. 1-(b). We remark that, in Fig. 1-(b), the arc-length locations of the cross-section on the inner and outer tubes are different (i.e., $s_m \neq s_k$) due to the relaxed concentricity. For any s_m on the inner tube (i.e., tube $i-1$), a mapping $f_{i-1}(s_m)$ is defined to find the corresponding arc-length position on the outer tube, s_k:

$$
s_k = f_{i-1}(s_m) = \operatorname*{argmin}_{\{s_k\},\ k=1,\dots,N_i} \|\mathbf{p}_i(s_k) - \mathbf{p}_{i-1}(s_m)\|_2 \tag{7}
$$

The mapping f_{i-1} in (7) is solved through Nearest Neighbor Search that finds the closest point $\mathbf{p}_i(s_k)$ for a given s_m. Once s_k

is found, the constraint is built on the cross-section perpendicular to the outer tube at s_k in terms of $\mathbf{p}_i(s_k)$ and $\mathbf{p}_{i-1}(s_m)$. The constraint $C(\mathbf{p}_{i-1}, \mathbf{p}_i)$ is constituted by collecting the constraint over all s_m on the inner tube.

The cross-section of tube $i-1$ at s_m, after projection into the outer tube's corresponding cross-section, should lie fully inside the latter, as shown in Fig. 1-(c). The centerline offset $\mathbf{p}_i(s_k) - \mathbf{p}_{i-1}(s_m)$ is projected to plane A as:

$$\mathbf{v} = \mathbf{P}_i(s_k)(\mathbf{p}_i(s_k) - \mathbf{p}_{i-1}(s_m)) \tag{8}$$

where $\mathbf{v}$ is the projected offset vector, and $\mathbf{P}_i(s_k)$ denotes the projection matrix of the cross-sectional plane, defined as

$$\mathbf{P}_i(s) = \mathbf{I} - \mathbf{p}_i'(s)\mathbf{p}_i'(s)^T. \tag{9}$$

When the two tubes are locally not parallel at the cross-section, there exists a non-zero angle θ between the tubes' tangential directions (see Fig. 1-(b)). In this case, the cross-sectional shape of the inner tube is an ellipsoid. By sliding the ellipsoid in contact with the outer tube along the circumference, it is inferred that $\mathbf{p}_{i-1}(s_m)$ is constrained inside an ellipsoidal trajectory S, as shown in Fig. 1-(c). The properties of minor and major axes of S are given by

$$\begin{aligned}\mathbf{q}_1 &= \langle \mathbf{P}_i(s_k)\mathbf{p}_{i-1}'(s_m)\rangle_2, \quad d_1 = r_i^{\text{in}} - \lambda_1 = r_i^{\text{in}} - r_{i-1}^{\text{out}}\\\mathbf{q}_2 &= \mathbf{q}_1 \times \langle \mathbf{p}_i'(s_k)\rangle_2, \quad d_2 = r_i^{\text{in}} - \lambda_2 = r_i^{\text{in}} - r_{i-1}^{\text{out}}\sec\theta\end{aligned} \tag{10}$$

respectively, where $\langle \cdot \rangle_2$ denotes the vector normalized w.r.t. L-2 norm, λ_1 and λ_2 are the lengths of the major and minor axes of the cross-sectional ellipsoid, $\mathbf{q}_1$ and $\mathbf{q}_2$ are the unit vectors that represents the direction of the major and minor axes , d_1 and d_2 are the lengths of the major and minor axes of ellipsoid S, and r_i^{in} and r_i^{out} are the inner and outer radii of tube i, respectively. The quadratic equation of S is given as $\mathbf{v}^T\mathbf{Q}\mathbf{v} = 1$, where $\mathbf{Q}$ at tube i, segment s_m is calculated by

$$\mathbf{Q}_{im} = \frac{1}{d_1^2}\mathbf{q}_1\mathbf{q}_1^T + \frac{1}{d_2^2}\mathbf{q}_2\mathbf{q}_2^T. \tag{11}$$

Therefore, the constraints on the tube pair can be obtained by combining (8) and (11) as

$$(\mathbf{p}_i(s_k) - \mathbf{p}_{i-1}(s_m))^T \; \mathbf{P}_i^T(s_k)\mathbf{Q}_{im}\mathbf{P}_i(s_k) \; (\mathbf{p}_i(s_k) - \mathbf{p}_{i-1}(s_m)) \leq 1 \tag{12}$$

The energy minimization is non-convex due to the non-convex constraints in (6c). By gradually increasing the intertube clearance, we can reduce the induced curvature and position deviation of the inner tube centerline, enabling the linearization of (6c). Suppose that, for a given inner radius of outer tube $\tilde{r}_i^{\text{in}}$, a feasible solution of (6) has already been attained as $\tilde{\mathbf{p}}^i$ and $\tilde{\mathbf{u}}^i$. Then the next sub-problem is defined by imposing a small deviation on clearance $r_i^{\text{in}} = \tilde{r}_i^{\text{in}} + \Delta c_i$. Assuming small $\Delta\mathbf{p}^i$ and $\Delta\mathbf{u}^i$ given a small Δc_i, a Jacobian mapping $\mathbf{J}_i$ can be found to linearize (6c) in the neighbourhood of $\tilde{\mathbf{u}}^i$ and $\tilde{\mathbf{p}}^i$. The resulting changes in the centerline and curvature are given by

$$\begin{aligned}\mathbf{p}^i &= \Delta\mathbf{p}^i + \tilde{\mathbf{p}}^i, \quad \mathbf{u}^i = \Delta\mathbf{u}^i + \tilde{\mathbf{u}}^i\\\Delta\mathbf{p}^i &= \mathbf{J}_i\Delta\mathbf{u}^i\end{aligned} \tag{13}$$

where $\mathbf{J}_i$ is obtained by taking derivative of (1) w.r.t. $\mathbf{u}_i$, the (k,j)-th block $\mathbf{J}_i(k,j)$ computed by:

$$\mathbf{J}_i(k,j) = \begin{cases} [\tilde{\mathbf{p}}_i(s_j) - \tilde{\mathbf{p}}_i(s_k)]_\times \mathbf{R}_i(s_j) & \text{if } k \geq j \\ \mathbf{0} & \text{if } k < j \end{cases} \tag{14}$$

For any adjacent tubes i and $i-1$, $\mathbf{Q}$ is updated with the increased r_i^{in}. Subsequently, we define two pairs of concatenated vectors as

$$\begin{aligned}\Delta\mathbf{u} &= [\Delta\mathbf{u}^{1^T}, ..., \Delta\mathbf{u}^{n^T}]^T, \quad \Delta\mathbf{p} = [\Delta\mathbf{p}^{1^T}, ..., \Delta\mathbf{p}^{n^T}]^T\\\tilde{\mathbf{u}} &= [\tilde{\mathbf{u}}^{1^T}, ..., \tilde{\mathbf{u}}^{n^T}]^T, \quad \tilde{\mathbf{p}} = [\tilde{\mathbf{p}}^{1^T}, ..., \tilde{\mathbf{p}}^{n^T}]^T\end{aligned} \tag{15}$$

By plugging (13)-(14) into (5) and 12 and ignoring the constant terms, the sub-problem for each increment in r_i^{in} is formulated as a minimization, of the form

$$\begin{aligned}\min_{\Delta\mathbf{u}} \quad & \left(\frac{1}{2}\Delta\mathbf{u}^T\mathbf{K}\Delta\mathbf{u} + (\tilde{\mathbf{u}} - \hat{\mathbf{u}})^T\mathbf{K}\Delta\mathbf{u}\right)\\\text{s.t.} \quad & \forall m = 1,2,\ldots,N_i, \quad i = 2,3,\ldots,n\\& \frac{1}{2}\Delta\mathbf{u}^T\mathbf{X}_{im}\Delta\mathbf{u} + \mathbf{Y}_{im}\Delta\mathbf{u} + \mathbf{Z}_{im} \leq 0,\\& \mathbf{X}_{im} = \mathbf{J}_{pi}^T\mathbf{S}_{im}^T\mathbf{P}_{im}^T\mathbf{Q}_{im}\mathbf{P}_{im}\mathbf{S}_{im}\mathbf{J}_{pi},\\& \mathbf{Y}_{im} = \tilde{\mathbf{p}}^T\mathbf{S}_{im}^T\mathbf{P}_{im}^T\mathbf{Q}_{im}\mathbf{P}_{im}\mathbf{S}_{im}\mathbf{J}_{pi},\\& \mathbf{Z}_{im} = \tilde{\mathbf{p}}^T\mathbf{S}_{im}^T\mathbf{P}_{im}^T\mathbf{Q}_{im}\mathbf{P}_{im}\mathbf{S}_{im}\tilde{\mathbf{p}} - 1,\\& \mathbf{J}_{pi} = \text{diag}(\mathbf{0},\cdots,\mathbf{0},\mathbf{J}_{i-1},\mathbf{J}_i,\mathbf{0},\cdots,\mathbf{0})\\& \mathbf{K} = \text{diag}(\mathbf{K}_1,...,\mathbf{K}_n)\\& \mathbf{S}_{im}\mathbf{p} = \mathbf{p}_{i-1}(s_m) - \mathbf{p}_i(f_{i-1}(s_m))\\& \mathbf{P}_{im} = \mathbf{I} - \mathbf{p}_i(f_{i-1}(s_m))\mathbf{p}_i'(f_{i-1}(s_m))^T.\end{aligned} \tag{16}$$

The problem can be simply viewed as a standard quadratically constrained quadratic programming problem (QCQP) over a variable $\Delta\mathbf{u}$. In this letter, the dual problem approach elaborated in [17] is used for solving the QCQP.

$$\begin{aligned}\max_{\lambda} \quad & -\frac{1}{2}\mathbf{q}(\lambda)^T\mathbf{P}(\lambda)^{-1}\mathbf{q}(\lambda) + \mathbf{r}(\lambda)\\\text{s.t.} \quad & \forall m = 1,2,...,N_i, \; i = 2,3,...,n, \; \lambda_{im} \geq 0\\& \mathbf{P}(\lambda) = \mathbf{K} + \sum_{i,m}\lambda_{im}\mathbf{X}_{im}\\& \mathbf{q}(\lambda) = \mathbf{K}^T(\tilde{\mathbf{u}} - \hat{\mathbf{u}}) + \sum_{i,m}\lambda_{im}\mathbf{Y}_{im}^T\\& \mathbf{r}(\lambda) = \sum_{i,m}\mathbf{Z}_{im}\end{aligned} \tag{17}$$

Specifically, at each step of clearance increment, the dual optimization problem (17), generated from primal problem (16) is optimized with respect to the vector λ. This problem comes with simpler constraints. After an optimal λ is reached, $\Delta\mathbf{u}$ could be efficiently computed by $\Delta\mathbf{u} = \mathbf{P}(\lambda)^{-1}\mathbf{K}(\tilde{\mathbf{u}} - \hat{\mathbf{u}})$, since $\Delta\mathbf{u}$ is must be the minimizer of Lagrangian. The whole large clearance solver could be formulated iteratively as summarized in Algorithm 1, where the initial condition is obtained using the conventional zero-clearance models [7].

C. Modeling of CTRs with Impulse Curvature

In this section, we will consider a more strict operation scenario when a tube is manipulated within a channel that has sudden curvature changes at certain places, such as the

Algorithm 1 Large clearance algorithm

   Initialize û
   ▷ Configure tube pre-curvature
   Initialize p̃, ũ
   ▷ Zero clearance initial guess from classic CTR models
   Initialize r^{in} N Δc
   ▷ Configure inner radius, number of incremental steps
   $step \leftarrow 1$
   while $step \leq N$ **do**
      Update mapping f from p̃
      Compute Jacobian **J** from p̃
      $r^{\text{in}} \leftarrow r^{\text{in}} + \Delta c$
      Compute **Q** from (10)(11)
      Solve (17) for optimal λ
      $\Delta \mathbf{u} \leftarrow \mathbf{P}^{-1}(\lambda)\mathbf{K}(\tilde{\mathbf{u}} - \hat{\mathbf{u}})$
      $\tilde{\mathbf{u}} \leftarrow \tilde{\mathbf{u}} + \Delta \mathbf{u}$
      Integrate ũ for updated shape p̃
      $step \leftarrow step + 1$
   end while
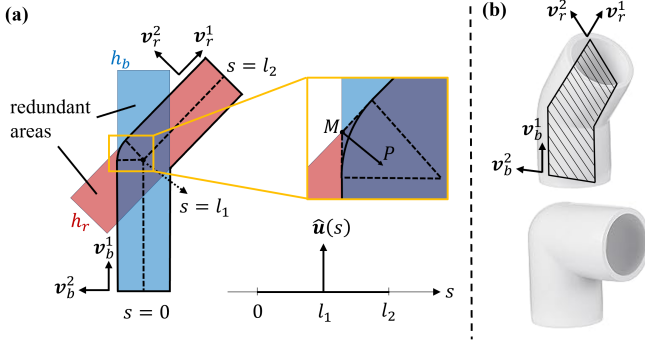
Fig. 2. Illustration of the tube with impulse curvature. (a). A schematic diagram that demonstrates the longitudinal section of the elbow joint. The change of the center line curvature with respect to arc-length along the elbow joint is also displayed. (b). Physical elbow joints used for pipe fittings. The corresponding longitudinal section in (a) is marked out.

bifurcation points along the blood vessel or sharp angles like elbow joints in pipelines. We term this sudden alteration in curvature as "impulse curvature". To illustrate, let's consider a complex outer tube that results from the fusion of two straight tubes, painted with red and blue color in Fig. 2). Curvature remains constant at 0 along red tube, experiences an abrupt transition to infinity at the juncture denoted by $s = l_1$, and then reverts to 0 along blue tube. Analogous to the concept of impulse input in control theory, we categorize this type of tube configuration as having an "impulse curvature". The combined assembly of the inner CTR and outer tube can be approximated as a subset of "concentric" tube robots. Notably, the outer tube exhibits significant clearance and possesses impulse curvature.

To model this type of CTRs, we efficiently view the elbow joint section as being formed by two intersecting straight sections, denoted as the red and blue areas in Fig. 2. While straight tubes are considered for presentation simplicity, they can be easily relaxed to non-straight smooth sections that are connected together. The inner tube segments are partitioned into three distinct regions: the blue area, the red area, and the overlapping area. We define three selection matrices, $\mathbf{B}, \mathbf{R}$, and $\mathbf{T}$, that leave only the elements of $\mathbf{p}$ included in the corresponding regions, respectively, and set the others to zero:

$$\mathbf{Bp} = [\mathbf{0}, \mathbf{0}, ..., \mathbf{p}(s_{t_1})^T, \mathbf{0}, ..., \mathbf{p}(s_{t_2})^T, ..., \mathbf{0}]^T_{3N_i \times 1}$$
$$\mathbf{Rp} = [\mathbf{0}, \mathbf{0}, ..., \mathbf{p}(s_{j_1})^T, \mathbf{0}, ..., \mathbf{p}(s_{j_2})^T, ..., \mathbf{0}]^T_{3N_i \times 1} \quad (18)$$
$$\mathbf{Tp} = [\mathbf{0}, \mathbf{0}, ..., \mathbf{p}(s_{l_1})^T, \mathbf{0}, ..., \mathbf{p}(s_{l_2})^T, ..., \mathbf{0}]^T_{3N_i \times 1}.$$

Let t, j and l represent the indices of inner tube segments situated within the blue, red, and overlapping regions, respectively. The constraints for the red and blue regions can be formulated analogously to (12) as

$$h_b(\mathbf{p}_1(s_t)) = \mathbf{p}^T \mathbf{S}_t^T \mathbf{P}_b^T \mathbf{Q} \mathbf{P}_b \mathbf{S}_t \mathbf{p} - 1 \leq 0,$$
$$h_r(\mathbf{p}_1(s_j)) = \mathbf{p}^T \mathbf{S}_j^T \mathbf{P}_r^T \mathbf{Q} \mathbf{P}_r \mathbf{S}_j \mathbf{p} - 1 \leq 0, \quad (19)$$
$$\mathbf{S}_{(\cdot)} \mathbf{p} = \mathbf{p}_1(s_{(\cdot)}) - \mathbf{p}_2(f_1(s_{(\cdot)})),$$

where the projection matrices to the cross sections of the blue and red sections are calculated using their tangential vectors $\mathbf{v}_b^1$ and $\mathbf{v}_r^1$ (see Fig. 2-(a)) as

$$\mathbf{P}_b = \mathbf{I} - \mathbf{v}_b^1 \mathbf{v}_b^{1^T}, \quad \mathbf{P}_r = \mathbf{I} - \mathbf{v}_r^1 \mathbf{v}_r^{1^T}. \quad (20)$$

In the overlapping area, applying both constraints at the same time can restrict the segments from moving out of the overlapping area during the iterative optimization. To avoid this situation, we consider the following disjunction constraint:

$$h_r(\mathbf{p}_1(s_l)) \leq 0 \text{ or } h_b(\mathbf{p}_1(s_l))) \leq 0, \quad (21)$$

or equivalently,

$$\min(h_r(\mathbf{p}_1(s_l)), h_b(\mathbf{p}_1(s_l))) \leq 0. \quad (22)$$

The feasible area of the above constraint covers all the colored regions in Fig. 2-(a), which unintentionally includes unnecessary redundant areas as indicated in the figure. We can cut them out using two planes (with normal vector $\mathbf{v}_b^2$ and $\mathbf{v}_r^2$) tangent to the cylinder of the blue and red section and perpendicular to the longitudinal plane, which gives the following directional constraint:

$$\overrightarrow{MP} \cdot \mathbf{v}_b^2 \leq 0, \quad \overrightarrow{MP} \cdot \mathbf{v}_r^2 \leq 0, \quad (23)$$

where M is a point on the intersection line of the segment planes, P is the point of the center line position $\mathbf{p}_1(s_l)$, and $\mathbf{v}_b^2$ and $\mathbf{v}_r^2$ are the unit normal vectors that represent the segment plane of blue and red section respectively.

We remark that the outer corner of the elbow joints is usually designed to be rounded in reality (Fig. 2-(b)) to enhance its durability and prevent the users from safety hazards. This rounded corner is not explicitly modeled since the directional constraint (23) already makes an approximation of the elbow joint in relatively high precision (Fig. 2-(a)). Simple modifications could be made to directional constraints for accommodation, should the rounded smooth outer corner be considered. Also, due to the inherent tendency of the inner tube to evolve its shape towards energy minimum, the inner tube normally does not make contact with the rounded outer corner.

Finally, we define $h_c(\mathbf{p}_1(s_l))$ as a combination of the constraints at the corner (22)-(23), and an energy minimization in the presence of the elbow joint is formulated as follows:

$$
\min_u \quad \frac{1}{2}(\mathbf{u}-\hat{\mathbf{u}})^T\mathbf{K}(\mathbf{u}-\hat{\mathbf{u}})
$$
$$
\begin{aligned}
\text{s.t.} \quad & h_b(\mathbf{p}_1(s_t)) = h_b(\mathbf{B}F(\mathbf{u})_t) \leq 0, \quad \forall t \in \{t_1,t_2,...\} \\
& h_r(\mathbf{p}_1(s_j)) = h_r(\mathbf{R}F(\mathbf{u})_j) \leq 0, \quad \forall j \in \{j_1,j_2,...\} \\
& h_c(\mathbf{p}_1(s_l)) = h_c(\mathbf{T}F(\mathbf{u})_l) \leq 0, \quad \forall l \in \{l_1,l_2,...\}
\end{aligned} \quad (24)
$$

In contrast to the previous case, this problem is not easily reduced to a QCQP due to the non-smooth constraint $h_c(\mathbf{p}_1(s_l))$. Alternatively, we adapt the Sequential Quadratic Programming (SQP), which sequentially approximates the problem as standard QPs and attains incremental solution updates. Each approximation undergoes differentiating constraints, which can be efficiently performed by using the Jacobian mapping in (14). With the introduction of Lagrangian multiplier λ, the corresponding Lagrangain function for this problem could be defined as:

$$
\begin{aligned}
L(\mathbf{u},\lambda) = & E_P(\mathbf{u}) + \sum_t \lambda_t(h_b((\mathbf{Bp})_t)) \\
& + \sum_j \lambda_j(h_r((\mathbf{Rp})_j)) + \sum_l \lambda_l(h_c((\mathbf{Tp})_l))
\end{aligned} \quad (25)
$$

For potential energy minimum to be reached, the necessary Karush–Kuhn–Tucker (KKT) conditions must be fulfilled, leading to the solution of equation $\nabla L(\mathbf{u},\lambda) = \mathbf{0}$ through Newton's method. Specifically, at iteration k, given a pair of feasible solutions $(\mathbf{u}^k,\lambda^k)$ and the corresponding $\mathbf{p}^k(=F(\mathbf{u}^k))$, the SQP subproblem can be formulated as follows:

$$
\min_{\mathbf{d}} \quad E_P(\mathbf{u}^k) + \nabla_{\mathbf{u}}E_P(\mathbf{u}^k)^T\mathbf{d} + \frac{1}{2}\mathbf{d}^T\nabla_{\mathbf{uu}}^2 L(\mathbf{u}^k)\mathbf{d}
$$
$$
\begin{aligned}
\text{s.t.} \quad & h_b((\mathbf{Bp}^k)_t) + \nabla_{\mathbf{u}}h_b((\mathbf{Bp}^k)_t)^T\mathbf{d} \leq 0 \\
& h_r((\mathbf{Rp}^k)_j) + \nabla_{\mathbf{u}}h_r((\mathbf{Rp}^k)_j)^T\mathbf{d} \leq 0 \\
& h_c((\mathbf{Tp}^k)_l) + \nabla_{\mathbf{u}}h_c((\mathbf{Tp}^k)_l)^T\mathbf{d} \leq 0 \\
& \mathbf{d} = \mathbf{u} - \mathbf{u}^k
\end{aligned} \quad (26)
$$

where

$$
\nabla_{\mathbf{u}}h_b(\mathbf{p}_m^k)^T = 2\mathbf{p}^{k^T}\mathbf{B}^T\mathbf{S}_m^T\mathbf{P}_b^T\mathbf{QP}_b\mathbf{S}_m\mathbf{BJ}
$$
$$
\nabla_{\mathbf{u}}h_r(\mathbf{p}_m^k)^T = 2\mathbf{p}^{k^T}\mathbf{R}^T\mathbf{S}_m^T\mathbf{P}_r^T\mathbf{QP}_r\mathbf{S}_m\mathbf{RJ}
$$
$$
\nabla_{\mathbf{u}}h_c(\mathbf{p}_l^k)^T = \mathbf{g}_l + \mathbf{TJV}_{b,l}^{2\,T} + \mathbf{TJV}_{r,l}^{2\,T}
$$
$$
\begin{aligned}
\nabla_{\mathbf{uu}}^2 L(\mathbf{u}^k) = & \mathbf{K} + \sum_t 2\lambda_t^k\mathbf{J}^T\mathbf{B}^T\mathbf{S}_t^T\mathbf{P}_b^T\mathbf{QP}_b\mathbf{S}_t\mathbf{BJ} \\
& + \sum_j 2\lambda_j^k\mathbf{J}^T\mathbf{R}^T\mathbf{S}_j^T\mathbf{P}_r^T\mathbf{QP}_r\mathbf{S}_j\mathbf{RJ} + \sum_l 2\lambda_l^k\mathbf{H}_l
\end{aligned} \quad (27)
$$
$$
\mathbf{J} = \begin{bmatrix} \mathbf{J}_1 & \mathbf{0} \\ \mathbf{0} & \mathbf{J}_2 \end{bmatrix}
$$
$$
\mathbf{V}_{b,l}^2 = [\mathbf{0}_{1\times3(l-1)},\ \mathbf{v}_b^{2\,T},\ \mathbf{0}_{1\times3(N_i-l)}]
$$
$$
\mathbf{V}_{r,l}^2 = [\mathbf{0}_{1\times3(l-1)},\ \mathbf{v}_r^{2\,T},\ \mathbf{0}_{1\times3(N_i-l)}]
$$

The gradient $\mathbf{g}_l$ and the hessian $\mathbf{H}_l$ of the disjunction constraint (22) in above equation are given by:

$$
\mathbf{g}_l = \begin{cases} \nabla_{\mathbf{u}}h_b(\mathbf{p}_l^k)^T, & h_b((\mathbf{Tp}^k)_l) \leq h_r((\mathbf{Tp}^k)_l) \\ \nabla_{\mathbf{u}}h_r(\mathbf{p}_l^k)^T, & h_r((\mathbf{Tp}^k)_l) < h_b((\mathbf{Tp}^k)_l) \end{cases}
$$
$$
\mathbf{H}_l = \begin{cases} \mathbf{J}^T\mathbf{B}^T\mathbf{S}_l^T\mathbf{P}_b^T\mathbf{QP}_b\mathbf{S}_l\mathbf{BJ}, & h_b((\mathbf{Tp}^k)_l) \leq h_r((\mathbf{Tp}^k)_l) \\ \mathbf{J}^T\mathbf{R}^T\mathbf{S}_l^T\mathbf{P}_r^T\mathbf{QP}_r\mathbf{S}_l\mathbf{RJ}, & h_r((\mathbf{Tp}^k)_l) < h_b((\mathbf{Tp}^k)_l) \end{cases}
$$
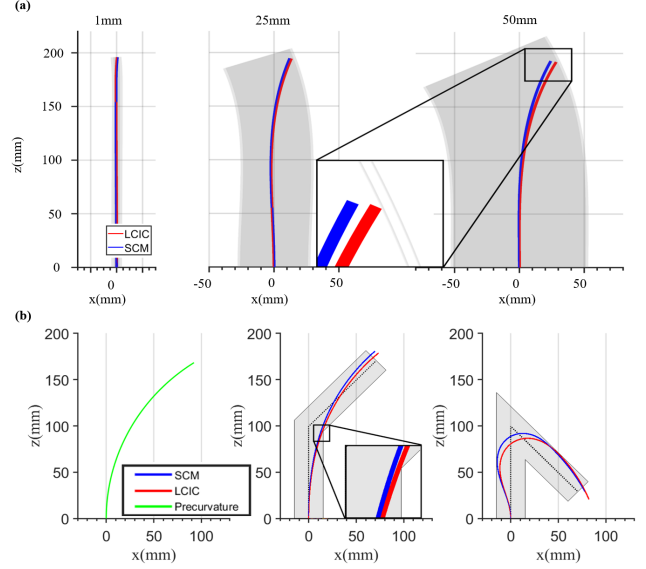
Fig. 3. Simulations of the proposed model at: (a). different outer tube inner radius, (b). different elbow with varying bending angle. In (a) the solution generated by LCIC model makes tip contact with the gray outer tube, while SCM fails to capture such property. In (b), for any chosen bending degree, LCIC model generates more feasible solutions compared to the conventional SCM.

after optimal $\mathbf{d}$ is reached, λ could be updated by solving:

$$
\nabla_{\mathbf{uu}}^2 L(\mathbf{u}^k)\mathbf{d} + \nabla h^T\lambda = -\nabla E_P(\mathbf{u}^k),
$$
$$
h = [h_b(\mathbf{p}_t^k),...,h_r(\mathbf{p}_j^k),...,h_c(\mathbf{p}_l^k)]^T
$$

Note that $\mathbf{B}$, $\mathbf{R}$, $\mathbf{T}$, and $\mathbf{S}_{(\cdot)}$ are simply constant matrices in this subproblem.

By employing this approach, the initial nonlinear optimization problem is effectively decomposed into a sequence of standard QPs with linear constraints and quadratic objectives defined in terms of $\mathbf{d}$. The resulting $\mathbf{d}$ is used to update $\mathbf{u}$ by $\mathbf{u}^{k+1} = \mathbf{u}^k + \mathbf{d}$. For practical implementation, the numerical optimization can be achieved using **fmincon** in Matlab with SQP as the underlying algorithm.

The iterative radius increment methodology, as previously introduced, can be incorporated together to handle the large clearance and impulse curvature simultaneously. This scenario involves two hierarchical iterative loops, the inner and outer loops of which are the SQP and the iterative radius increment, respectively. For each subproblem of the SQP, the mapping f, $\mathbf{B}$, $\mathbf{R}$, and $\mathbf{T}$ are updated prior to solving (26). This adjustment is essential due to the dynamic evolution of the inner tube's centerline during the SQP.

The method proposed in [12] is used to provide the initial solution for the very first QP. For this purpose, as the method in [12] only allows finite tube curvatures, the elbow joint of the outer tube was relaxed into a smooth curve with finite curvature.

III. RESULTS AND DISCUSSIONS

In this section, we will first validate the proposed large clearance and impulse curvature model in numerical simulation. Then we will perform benchtop experiment validations

TABLE I
TUBE PARAMETERS FOR NUMERICAL EXPERIMENTS

Scenario	Large Clearance		Impulse Curvature	
Tube	Outer	Inner	Outer	Inner
Length [mm]	200	200	200	200
Bending Stiffness [Nm^2]	20	20	Inf	20
Poisson's Ratio	0.3	0.3	0.3	0.3
Precurvature [m^{-1}]	0.005	0.005	0	0.005
Outer Tube ID [mm]	Var	0	30	0
Inner Tube OD [mm]	-	1.32	-	1.32

to show the performance of the proposed method and the improvement compared to the state-of-the-art approaches.

A. Numerical Simulation Studies

Two operation scenarios are considered with different shapes of the outer tube, corresponding to the proposed large curvature model in Sec.II-B and the impulse curvature model in Sec.II-C:

1) **Large clearance**. The inner diameter of the outer tube is selected to be 3.32 mm, 51.32 mm, and 101.32 mm in order to represent both small and large clearance scenarios. The inner and outer tubes are subjected to the axial rotation angle of $180°$ at the base.

2) **Impulse curvature**. Here, we consider the inner tube operating inside a pipe that has an elbow joint of $\{45°, 135°\}$, respectively.

The tube properties used in both scenarios are presented in Table I. Note that in the impulse curvature scenario, the outer tube is rigid with a shape of elbow joints.

Fig. 3-(a) presents the outcomes of our LCIC model applied to superelastic Nitinol CTRs with a large outer tube, with a comparison to the small clearance model (SCM) developed in [12]. With small clearance, both models are able to achieve comparable performance. However, with the increased clearance, it is clear that our LCIC model is more accurate in predicting the inner tube behavior. Specifically, the distal tip contact is precisely described with the LCIC model, but the SCM fails. In Fig. 3-(b), we showcase the results when a superelastic tube is operating inside a pipe that has an impulse curvature along the body. The proposed model successfully generates feasible configurations subject to various connection angles. Since the impulse curvature scenario in Sec. II-C is not considered in [12], the SCM simply treats the overlapping segments in (18) as $\mathbf{Tp} = \mathbf{0}_{\{3N_i \times 1\}}$ and removes the corner constraint (22) in the optimization problem (24).The resulting inner tube shape generated from SCM in $45°$ senario (Fig. 3-(b): middle) is physically unachievable. It is obvious that the tube is deformed compared to its original shape, which indicates forces/contacts being applied at certain points along the tube, but simulation results indicate no contact between the inner tube and outer channel is observed.

B. Experimental Validation

In this section, we want to present the experimental validations of our LCIC model with a pre-shaped superelastic Nitinol

tube operating at different scenarios. The tube parameters are given in Table II. Both LCIC and SCM models are implemented for comparative study. In all experiment, the accuracy of the models is evaluated from three performance indices: the distal tip error e_{tip}, the average whole-body error e_{mean}, and the maximum whole-body error e_{max}, which are defined as

$$e_{\text{tip}} = \mathbf{p}_1(s_{N_1}) - \mathbf{p}_{1,\text{ex}}(s_{N_1})$$

$$e_{\text{mean}} = \frac{1}{N_1} \sum_{i=1}^{N_1} \|\mathbf{p}_1(s_i) - \mathbf{p}_{1,\text{ex}}(s_i)\|_2 \quad (28)$$

$$e_{\text{max}} = \max_{i \in 1,...,N_1} \|\mathbf{p}_1(s_i) - \mathbf{p}_{1,\text{ex}}(s_i)\|_2$$

where $\mathbf{p}_1(s_i)$, $\mathbf{p}_{1,\text{ex}}(s_i)$ denotes the position of the i-th discretization point of the inner tube, from the model result and experimental result, respectively.

TABLE II
PARAMETERS OF THE INNER TUBE

ID \ OD	Total Length	Bending Stiffness	Poisson's ratio
0.91 \ 1.32 mm	213.88 mm	20.07 Nm^2	0.3

1) Planar Scenario: We first operate the pre-shaped Nitinol tube inside a 2D channel with a large clearance and a right angle (impulse curvature) (see Fig. 4). To simplify the experimental workflow and enable accurate shape measurement of the curved inner tube, the channel is fabricated with 3D printing technique with a thickness equal to the tube diameter, leading to the planar deformation of the inner tube when operating within. The channels have three different inner radii r_2 of 5 mm, 10 mm, and 15 mm, respectively. For each channel, the inner tube is manually inserted with 3 different insertion depths, measured via a digital calibrator (resolution: 0.1mm). This will result in a total of 9 groups of experimental data. Note that the tube shape in both free- and constrained-condition is captured via camera (4032×3024 pixel resolution). To transform the shape data from the camera frame to the global frame, we choose 7 control points with known global positions on the channel (see Fig. 4-b) to perform the coordinate registration (mean registration error: 0.4 mm).

As shown in Table III, the LCIC provides an more accurate estimation of the tube shape than the SCM in all groups of experimental data, especially when the clearance becomes larger. The average tip position error of the LCIC across all groups are 1.53 mm, which provides an improved accuracy of 71% compared to the 5.34 mm average error of the SCM.

The modeled shape and measured shape is detailed in a representative setting that has a large clearance and impulse curvature (see Fig. 5). The zoom-in plot in Fig 5 demonstrates the contact details of the inner tube located at the corner. Since the centerline of the outer pipe consists of an impulse curvature ($90°$ corner), the projection matrix $\mathbf{P}_i(s)$ in (9) changes drastically when the the inner tube enters another section of the elbow joint and therefore the contact constraints (12) shifts. The length of the center line is denoted as l_m for the vertical cylinder. The SCM assumes that the shift of constraints takes place at $s = l_m$, while in reality $s < l_m$ due to the large
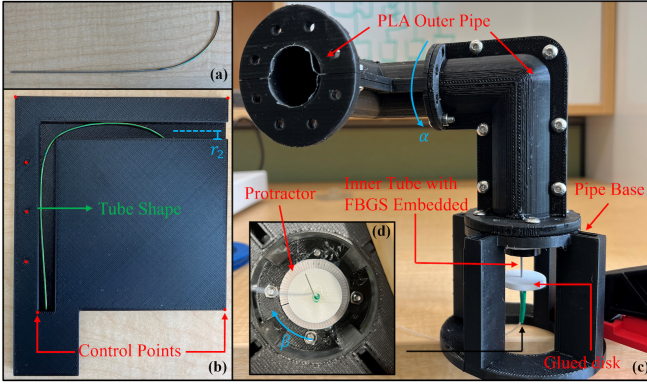
Fig. 4. Experiment validations of the CTR clearance model. (a). The original shape of the precurved tube. (b). A planar scenario where a curved tube was inserted into a grooved PLA channel with a inner radi of r_2. The control points (red) with known global positions were used for image registration. The shape of the tube inside the outer pipe (green) was extracted by sampling the points in the image manually. (c). A 3D scenario. The outer channel consisted of two bending segments that could rotate with respect to each other, and a disk was glued to the inner tube to control the orientation. (d). The bottom view of the 3D scenario. The rotation angle of the bending segments and the inne tube is labeled as α and β respectively.
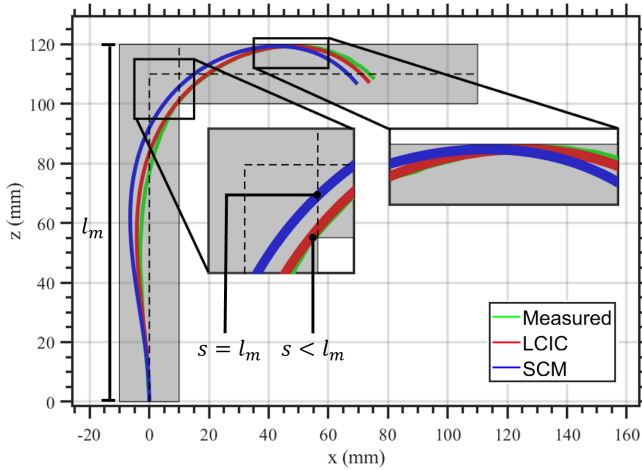
Fig. 5. Representative experimental results of a precurved tube in a 90-degree-bent rigid planar pipe (green outline). The result shows a comparison between the shape estimated by SCM, , and the measured shape in experiments. The zoom-in plot near the corner/top region of the outer pipe are also displayed.

clearance. This leads to stricter constraints of the SCM at the corner and therefore the failure to model the contact. On the contrary, the disjunction constraint (22) of the LCIC fits both the horizontal and vertical section of the elbow joint, and accurately predicts the contact behaviors of the inner tube at the corner.

2) 3D Scenario: In this section, we want to evaluate the efficacy of the proposal model in a more complicated operation scenario, where the Nitinol inner tube is manipulated within a 3D channel that has an out-of-plane bending segment (Fig. 4 shows that an out-of-plane bending segment is perpendicular to the plane that is defined by the other segments). To generate various shapes of the outer channel, the out-of-plane segment is able to rotate relatively with respect to the others and fixed using screws at angles of $\alpha = -45°, 0°, 45°$ (refer to Fig.6-(a)-(c). This operation scenario can be found in many engineering

TABLE III
ERROR ANALYSIS IN 2D PLANAR SCENARIO

r_2 [mm]	l_1 [mm]	e_{tip} [mm] SCM	e_{tip} [mm] LCIC	e_{mean} [mm] SCM	e_{mean} [mm] LCIC	e_{max} [mm] SCM	e_{max} [mm] LCIC
5	152.76	3.56	2.17	1.09	0.66	3.56	2.17
	167.78	1.45	0.87	0.80	0.43	1.45	0.89
	177.42	1.81	0.75	0.78	0.34	1.62	1.04
10	158.38	5.38	1.54	2.62	0.61	5.38	1.54
	166.67	6.53	1.99	2.86	0.80	6.53	1.99
	176.93	5.95	1.86	2.61	0.85	5.95	2.13
15	157.04	6.22	0.56	3.41	0.48	6.22	0.84
	166.76	8.67	2.42	4.14	0.78	8.67	2.42
	176.32	8.49	1.58	4.51	0.81	8.49	1.94

applications such as pipe inspection. Plastic tape is applied on the inner wall surface to reduce friction. Due to limited visibility inside the pipe during the experiment, Fiber Bragg Grating (FBG) sensors are chosen instead of imaging systems to measure the shape of the inner tube. Similarly, the inner tube insertion is manually controlled with 4 different lengths, leading to a total of 12 groups of experimental results. A PLA disk is glued to the inner tube, and a protractor fixed at the base is used to measure the tube's rotation angle β.

$$[\mathbf{p}_{1,\text{ex}}^T(s), 1]^T = \mathbf{T} \ [\mathbf{p}_{1,\text{fbg}}^T(s), 1]^T \quad (29)$$

The registration is implemented in Matlab using iterative closest point algorithm, and the maximum error is 2.0 mm.

The error metrics e_{tip}, e_{mean}, and e_{max} of both SCM and LCIC models in the 3D experiments are presented in Table IV. In all groups of experimental results, the prediction of the LCIC shows significant decreased errors compared to that of the SCM. The average tip position error of the LCIC across all groups is 4.36 mm. Comparing to the 12.64 mm average error of the SCM, 66% improvement of the model accuracy is reported. The maximum body error of LCIC among all the groups is 4.90 mm, which corresponds to 2.73% of the total arc length. Fig. 6 depicts the shapes of inner tube inside the three different 3D pipes corresponding to $\alpha = 45°, 0°, -45°$. In all cases, the shapes predicted by the LCIC model fit well with the experimental data compared to that of the SCM. No contact is observed at the unmodeled outer corners. The LCIC model precisely captures the contact positions at both corners in Fig 6-(a) because the contact constraints proposed in (12), (22), and (23) are more accurate compared to the existing model.

IV. CONCLUSION

In this letter, we present the CTR robot model that can accommodate the large clearance and impulse curvature. The proposed method demonstrates increased accuracy compared to the existing small clearance model in both 2D planar and 3D operation scenarios, leading to a tip position error of 1.53 mm and 4.36 mm, outperforming the state-of-the-art by 71% and 66%, respectively. This proposed LCIC model makes one step further to the precise modeling of CTRs, with the prospect for applications inside large channels such as aorta, lung bronchi, and industrial pipes.
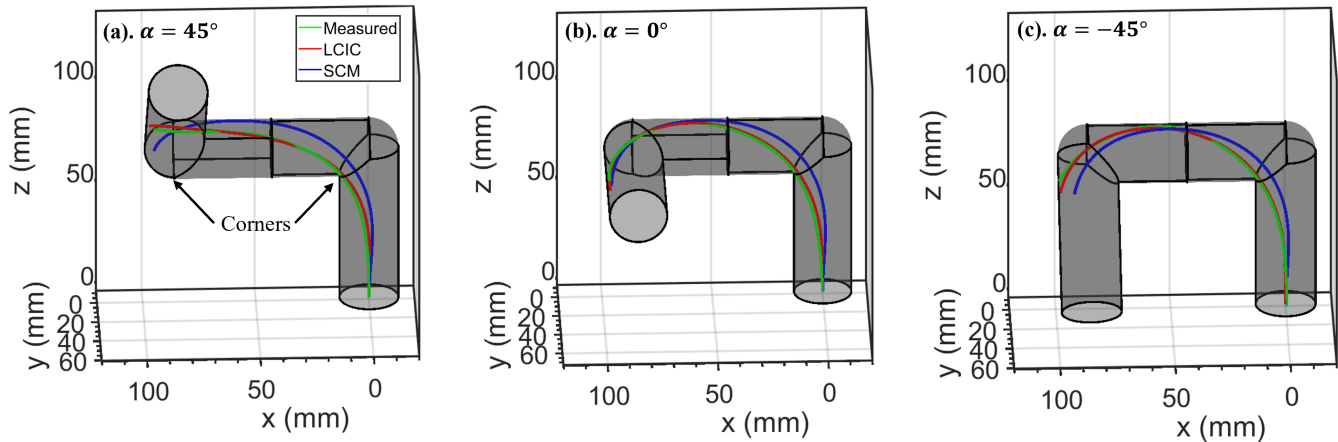
Fig. 6. Representative experimental results of a precurved tube in a rigid 3D pipe with 90° elbow joints. The result shows a comparison between the shape estimated by SCM, LCIC, and the measured shape in experiments.

TABLE IV

ERRORS OF 3D RIGHT ANGLE PIPE MODEL

α [°]	β [°]	l_1 [mm]	e_{tip} [mm] SCM	e_{tip} [mm] LCIC	e_{mean} [mm] SCM	e_{mean} [mm] LCIC	e_{max} [mm] SCM	e_{max} [mm] LCIC
45	150	176.38	16.98	3.18	6.45	1.97	16.97	4.18
45	150	179.52	19.72	3.06	6.56	2.15	19.72	4.90
45	150	182.89	16.63	2.85	6.38	1.47	16.63	2.92
45	150	184.98	14.53	3.40	5.08	1.81	14.53	4.03
-45	85	176.38	10.76	4.94	4.61	2.05	9.97	4.23
-45	85	179.52	6.75	4.95	3.62	1.64	6.77	4.76
-45	85	182.89	11.65	4.59	3.26	1.22	11.63	3.79
-45	85	184.98	7.65	5.46	2.98	1.17	7.63	3.74
0	115	176.38	11.71	5.35	4.08	1.98	11.13	3.97
0	115	179.52	13.89	4.16	4.34	1.73	13.51	3.56
0	115	182.89	10.75	5.36	4.38	1.80	10.50	4.03
0	115	184.98	10.61	4.98	3.92	1.54	10.61	4.11

REFERENCES

[1] P. E. Dupont, N. Simaan, H. Choset, and C. Rucker, "Continuum robots for medical interventions," *Proceedings of the IEEE*, vol. 110, no. 7, pp. 847–870, 2022.

[2] C. Kim, A. Ataollahi, I. Berra, and P. Dupont, "Cardioscopic imaging to guide manual and robotic surgery inside the beating heart," in *Hamlyn Symposium on Medical Robotics*, pp. 15–16, Citeseer, 2015.

[3] E. J. Butler, R. Hammond-Oakley, S. Chawarski, A. H. Gosline, P. Codd, T. Anor, J. R. Madsen, P. E. Dupont, and J. Lock, "Robotic neuro-emdoscope with concentric tube augmentation," in *2012 IEEE/RSJ international conference on intelligent robots and systems*, pp. 2941–2946, IEEE, 2012.

[4] P. E. Dupont, J. Lock, B. Itkowitz, and E. Butler, "Design and control of concentric-tube robots," *IEEE Transactions on Robotics*, vol. 26, no. 2, pp. 209–225, 2009.

[5] P. E. Dupont, J. Lock, and E. Butler, "Torsional kinematic model for concentric tube robots," in *2009 IEEE International Conference on Robotics and Automation*, pp. 3851–3858, IEEE, 2009.

[6] D. C. Rucker, B. A. Jones, and R. J. Webster III, "A geometrically exact model for externally loaded concentric-tube continuum robots," *IEEE Transactions on Robotics*, vol. 26, no. 5, pp. 769–780, 2010.

[7] P. E. Dupont, J. Lock, B. Itkowitz, and E. Butler, "Design and control of concentric-tube robots," *IEEE Transactions on Robotics*, vol. 26, no. 2, pp. 209–225, 2010.

[8] P. E. Dupont, J. Lock, and B. Itkowitz, "Real-time position control of concentric tube robots," in *2010 IEEE International Conference on Robotics and Automation*, pp. 562–568, IEEE, 2010.

[9] D. C. Rucker and R. J. Webster, "Computing jacobians and compliance matrices for externally loaded continuum robots," in *2011 IEEE International Conference on Robotics and Automation*, pp. 945–950, IEEE, 2011.

[10] M. N. Boushaki, C. Liu, and P. Poignet, "Task-space position control of concentric-tube robot with inaccurate kinematics using approximate jacobian," in *2014 IEEE International Conference on Robotics and Automation (ICRA)*, pp. 5877–5882, 2014.

[11] Y. Ding, X. Wang, H. Kuang, and K. Xu, "Incorporating trocar clearance in the kinematics of multi-backbone continuum robots for single-port surgery," in *2022 IEEE International Conference on Robotics and Biomimetics (ROBIO)*, pp. 1757–1762, IEEE, 2022.

[12] J. Ha and P. E. Dupont, "Incorporating tube-to-tube clearances in the kinematics of concentric tube robots," in *2017 IEEE International Conference on Robotics and Automation (ICRA)*, pp. 6730–6736, 2017.

[13] J. Ha, G. Fagogenis, and P. E. Dupont, "Modeling tube clearance and bounding the effect of friction in concentric tube robot kinematics," *IEEE Transactions on Robotics*, vol. 35, no. 2, pp. 353–370, 2018.

[14] T. Liu, G. Zhang, P. Zhang, T. Cheng, Z. Luo, S. Wang, and F. Du, "Modeling of and experimenting with concentric tube robots: Considering clearance, friction and torsion," *Sensors*, vol. 23, no. 7, p. 3709, 2023.

[15] A. Hager, H. Kaemmerer, U. Rapp-Bernhardt, S. Blücher, K. Rapp, T. M. Bernhardt, M. Galanski, and J. Hess, "Diameters of the thoracic aorta throughout life as measured with helical computed tomography," *The Journal of thoracic and cardiovascular surgery*, vol. 123, no. 6, pp. 1060–1066, 2002.

[16] D. C. Rucker, B. A. Jones, and R. J. Webster III, "A geometrically exact model for externally loaded concentric-tube continuum robots," *IEEE transactions on robotics*, vol. 26, no. 5, pp. 769–780, 2010.

[17] S. P. Boyd and L. Vandenberghe, *Convex optimization*. Cambridge university press, 2004.